The Astrophysical Journal, 843:152 (12pp), 2017 July 10 https://doi.org/10.3847/1538-4357/aa7946

Determinations of the $^{12}C/^{13}C$ Ratio for the Secondary Stars of AE Aquarii, SS Cygni, and RU Pegasi*

Thomas E. Harrison and Rachel E. Marra
Department of Astronomy, New Mexico State University, Box 30001, MSC 4500, Las Cruces, NM 88003-8001, USA
tharriso@nmsu.edu, rmarra@nmsu.edu
Received 2017 February 20; revised 2017 June 5; accepted 2017 June 11; published 2017 July 14

Abstract

We present new moderate-resolution near-infrared spectroscopy of three CVs obtained using GNIRS on Gemini-North. These spectra covered three ^{13}CO bandheads found in the *K*-band, allowing us to derive the isotopic abundance ratios for carbon. We find small $^{12}C/^{13}C$ ratios for all three donor stars. In addition, these three objects show carbon deficits, with AE Aqr being the most extreme ($[C/Fe] = -1.4$). This result confirms the conjecture that the donor stars in some long-period CVs have undergone considerable nuclear evolution prior to becoming semi-contact binaries. In addition to the results for carbon, we find that the abundance of sodium is enhanced in these three objects, and the secondary stars in both RU Peg and SS Cyg suffer magnesium deficits. Explaining such anomalies appears to require higher mass progenitors than commonly assumed for the donor stars of CVs.

Key words: infrared: stars – novae, cataclysmic variables – stars: abundances – stars: individual (AE Aqr, SS Cyg, RU Peg)

1. Introduction

A cataclysmic variable (CV) consists of a cool, low-mass secondary that fills its Roche lobe and transfers material to a white dwarf primary. The standard evolutionary paradigm has the more massive component in the binary evolve off the main sequence and engulf its companion in a short-lived common envelope (CE) phase (e.g., Iben & Livio 1993). During the CE phase, the outer atmosphere of the primary star is ejected by interaction with the secondary star, and the result is either a stellar merger or a compact binary (Politano & Weiler 2007). Angular momentum loss processes slowly shorten the period until it becomes a semi-contact binary. One outstanding question in this picture is whether there are any CVs where the donor stars have undergone significant evolution prior to contact. In earlier population studies, the expectation was that chemical evolution was not important (see Howell et al. 2001 and references therein). In more recent studies, such as those by Podsiadlowski et al. (2003) and Goliasch & Nelson (2015), pre-contact chemical evolution was considered. Goliasch & Nelson found that the large spread in donor star spectral type for longer period CVs (c.f., Beuermann et al. 1998) is easily explained by assuming a range in evolutionary states at the time of contact.

Podsiadlowski et al. suggest that the presence of CNO cycle processed elements in the photospheres of CV donors would be strong evidence for pre-contact evolution. There has been plenty of evidence for carbon deficits in the donor stars of CVs (see Harrison 2016 and references therein). There is also evidence for unusual nitrogen to carbon emission line ratios in the UV spectra of CVs (e.g., Gänsicke et al. 2003). Hamilton et al. (2011) found a one-to-one correlation in that CVs with carbon-deficit donor stars also have enhanced nitrogen emission. These are the hallmarks of the CNO cycle, but apparently, such results have not proven to be sufficient to clinch the case for nuclear evolved donors. A more robust result would be the detection of isotopic ratios in CNO species in the donor star, such as $^{12}C/^{13}C$, that can only arise from nuclear processing.

Kalomeni et al. (2016) followed the evolution of a large number of systems to investigate the pathways that result in the birth of a CV system. This study was not a population synthesis, thus it did not impose limits on the properties of the primordial binaries. In this way, they could trace back an end result to find the binary that the CV descended from. One of the findings of this study was that many of the CVs that had donors that were evolving off the main sequence before becoming semi-contact binaries ended up with extremely low levels of carbon and highly enhanced levels of nitrogen. This was due to the CNO bi-cycle, where the CN leg runs, while the NO portion does not. This causes highly depleted levels of ^{12}C but huge enhancements of ^{14}N, with N/C ratios that are 100× the cosmic value. In the CN cycle, ^{13}C is produced as a precursor to ^{14}N. If the CN cycle is run to completion, the final $^{12}C/^{13}C$ ratio is four (Wollman 1973). Harrison (2016) has noted the evidence for the presence of ^{13}CO absorption features in the donor stars of several CVs and demonstrated that U Gem appears to have a value for the $^{12}C/^{13}C$ ratio that suggests the CN cycle has run to completion in that object.

Even if such enhancements are common, it remains challenging to obtain adequate data to investigate the $^{12}C/^{13}C$ ratio in the donor stars of CVs. Below we describe new moderate-resolution *K*-band spectroscopy of three cataclysmic variables that were previously shown to have donor stars that have non-solar values for their carbon abundance. In all three cases, ^{13}CO absorption appears to be present, suggesting an overabundance of this isotope. Even more surprising, however, is that sodium is clearly enhanced in all three secondary stars. In the next section, we describe the observations. In Section 3, we present our results, with the summary and conclusions in Section 4.

* Based on observations obtained at the Gemini Observatory, which is operated by the Association of Universities for Research in Astronomy, Inc., under a cooperative agreement with the NSF on behalf of the Gemini partnership: the National Science Foundation (United States), the National Research Council (Canada), CONICYT (Chile), Ministerio de Ciencia, Tecnología e Innovación Productiva (Argentina), and Ministério da Ciência, Tecnologia e Inovação (Brazil).

Table 1
Observation Log

Object	UT Date	Start/Stop Times (UT)	Num. Exp. × Exp. Time	Airmass	V	Obs. Phase
AE Aqr	2016 May 17	14:32 to 14:53	16 × 60 s	1.08	11.3	0.15
SS Cyg	2016 Apr 19	14:44 to 15:11	16 × 100 s	1.45	8.7	0.09
SS Cyg	2016 Apr 25	08:55 to 09:21	16 × 100 s	1.51	10.5	0.28
SS Cyg	2016 Apr 26	14:20 to 14:25	2 × 100 s	1.51	10.8	0.94
RU Peg	2016 Apr 26	14:44 to 15:07	16 × 90 s	1.50	12.5	0.46
HD209932	2016 Apr 25	14:46 to 14:50	6 × 10 s	1.51	6.5	N/A
HD210501	2016 Apr 26	14:35 to 14:37	3 × 10 s	1.60	7.7	N/A
HD198070	2016 May 17	14:19 to 14:22	3 × 10 s	1.09	6.4	N/A

2. Data

The observations were made with GNIRS[1] on Gemini-North. The 111 line mm^{-1} grating was used to obtain spectra that covered the wavelength range 2.2317 μm $\leqslant \lambda \leqslant$ 2.420 μm, with a dispersion of 1.84 Å $pixel^{-1}$. Three ^{13}CO bandheads are covered by these spectra. These data were flatfielded, and spectra extracted and wavelength calibrated using the normal process in IRAF. Telluric correction stars were observed immediately before, or right after, the observation of the target to minimize the differences in airmass.

The observation log is presented in Table 1, where we detail the date and time of the observations, the number of individual exposures and their duration, the mean airmass of the observing sequence, the V magnitude of the target, and the mean orbital phase of the CV. We also list the telluric standard star observation log for completeness. Instead of using an ephemeris to Doppler-correct these data, we simply measured the positions of strong atomic features and then shifted the spectra for each object so that they overlapped before median-combining them. All three targets have long orbital periods, and the total integration time spent on each was relatively brief.

The red end of the K-band has very strong telluric absorption features (see Figure 1) that can change rather rapidly with time. Unfortunately, only a single telluric standard was obtained to correct the data set for each object. Thus, even though close in airmass, there remain residuals in the final telluric-corrected spectra. This is especially true of the region near the $^{13}CO_{(3,1)}$ bandhead at 2.374 μm.

There were multiple observations of SS Cyg. The first of these occurred on 2016 April 19, right at the peak of an outburst. These data are partially saturated. No telluric standard was observed that night. The second epoch of data for SS Cyg was obtained according to the observation request. An additional two spectra of SS Cyg were obtained on 2016 April 26 (for unknown reasons). We have used the standard star obtained on that night for RU Peg to reduce these two spectra and have median-combined them with the 16 spectra of SS Cyg obtained on 2016 April 25.

3. Abundance Measures and Their Errors

In the following, we will be generating grids of synthetic spectra using the programs and procedures outlined in Harrison (2016). We use the program SPECTRUM by R. Gray[2] to generate model spectra. As noted in Harrison & Hamilton (2015) and Harrison (2016, hereafter "H16"), the line list for the red end of the K-band is still incomplete due to the presence of strong CO absorption features in the spectra of the template stars. It requires higher resolution data than we have yet obtained to properly verify the ability of the current line list to reproduce observations. Thus, some spectral features seen in the GNIRS data are not well modeled by the current line list. These lines, however, are generally only visible due to the weakness of the CO features in the target CVs.

In the analysis of the abundances for this paper, we again use χ^2 analysis covering both large and small wavelength ranges, depending on the goals of the analysis. In Harrison & Hamilton (2015), synthetic K-band spectra were produced using MOOG (Sneden 1973) to derive $T_{\rm eff}$, [Fe/H], and [C/Fe] for three CVs. The 1σ error bar on [Fe/H] quoted for their analysis was ±0.25, while for $T_{\rm eff}$ the error bar was ±250 K. To arrive at those values, synthetic spectra were generated so as to model K dwarfs from the IRTF Spectral Library (Cushing et al. 2005).

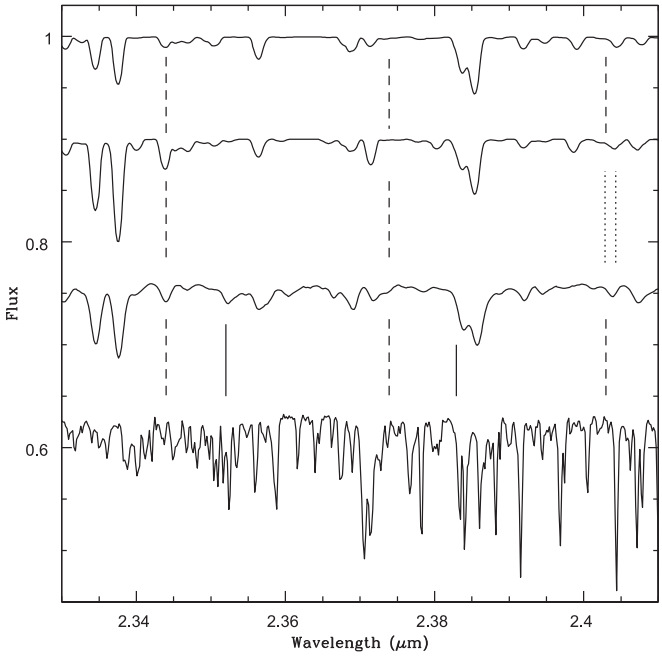

Figure 1. The two spectra plotted at the top are models where the carbon abundance has been set to zero so as to highlight the effect of Ti I absorption on the ^{13}CO bandhead at 2.345 μm (the locations of the ^{13}CO bandheads are indicated by vertical dashed lines). The topmost spectrum has $T_{\rm eff}$ = 5000 K, while the other spectrum has $T_{\rm eff}$ = 4000 K. The spectrum below that is of AE Aqr, which appears to have strong ^{13}CO absorption and very weak ^{12}CO bandheads (vertical solid lines). The dotted lines locate a weak Na I doublet that complicates the modeling of the $^{13}CO_{(4,2)}$ bandhead. The bottom spectrum is that of a telluric correction standard and shows the locations of the deepest telluric features that may leave residuals in the reduced data for the three CVs.

[1] https://www.gemini.edu/sciops/instruments/gnirs/
[2] http://www.appstate.edu/~grayro/spectrum/spectrum.html

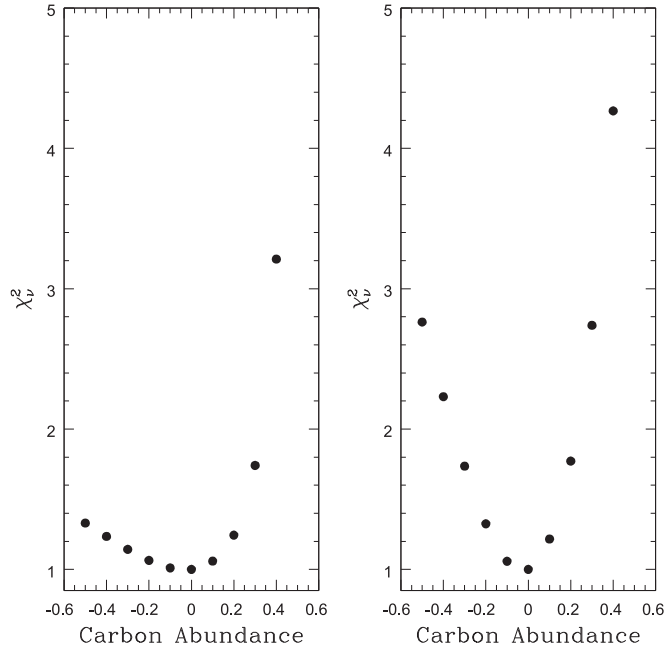

Figure 2. Values of χ^2_ν for different values of the carbon abundance for HD 3765, covering the range $-0.5 \leqslant [C/Fe] \leqslant +0.5$. The left-hand panel is for the spectral range 2.1825 μm $\leqslant \lambda \leqslant$ 2.3775 μm, and the right-hand panel is for the spectral range 2.2825 μm $\leqslant \lambda \leqslant$ 2.3775 μm.

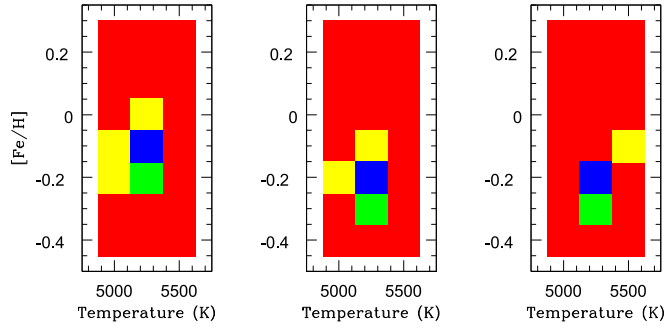

Figure 3. Heat map for the metallicity and temperature fits to the *K*-band spectrum of HD 10476. The leftmost panel is for the wavelength range 2.08 to 2.14 μm, the middle panel is for 2.19 to 2.29 μm, and the rightmost panel is for 2.21 to 2.29 μm. In this, and similar figures that follow, red symbolizes results where χ^2_ν is $>3\sigma$, yellow for $2\sigma < \chi^2_\nu \leqslant 3\sigma$, green for $1\sigma < \chi^2_\nu \leqslant 2\sigma$, and blue for $\chi^2_\nu \leqslant 1\sigma$.

The standard deviations on the values of [Fe/H] for the means of the previously published values for the IRTF spectral templates were all of order $\pm$0.10, while their temperatures were typically good to $\pm$100 K. The final model error bars for the K dwarfs that were quoted in Harrison & Hamilton for [Fe/H] and $T_{\rm eff}$ resulted from analysis of spectral ranges that excluded the CO features, as those features were peculiar in the CVs under study. If we had incorporated the CO features into the analysis of the K-dwarf spectra, the error bars on the derived values of [Fe/H] and $T_{\rm eff}$ would have been smaller. Because we could not analyze the CVs this way, we quoted the more conservative error bars derived from regions blueward of 2.29 μm. As we show below, given the strength of the CO features in the *K*-band spectra of K dwarfs, the measurement of [C/Fe] was far more robust than that for [Fe/H]. Thus, we simply quoted the error bars on [Fe/H] for [C/Fe].

In H16, the program SPECTRUM was used to generate synthetic spectra from 0.80 μm to 2.5 μm to allow the modeling of cross-dispersed data obtained using SPEX on the IRTF or TripleSpec on the Apache Point Observatory 3.5 m. By modeling the *IJHK* bandpasses independently of each other and averaging the results, they were able to improve the precision on the metallicity measurement to $\pm$0.10 and on the temperature to $\pm$110 K. We now demonstrate how the ability to constrain the measurement of [C/Fe] rests on the uncertainty in [Fe/H]. In Figure 2, we present the χ^2 analysis for the CO features in the K2 dwarf HD 3765. As shown in Table 2 of H16, the nominal values for its temperature and metallicity are 5023 $\pm$ 66 K and $+0.05 \pm 0.10$, respectively. To perform the following analysis, we used a Kurucz model atmosphere with $T_{\rm eff} = 5000$ K and [Fe/H] = 0.0. A grid, with the metallicity and temperature fixed to these values, was constructed with the carbon abundance varying over the range $\pm$0.5 (in dex).

The left-hand panel of Figure 2 shows the result for a broad region of the *K*-band from 2.1825 μm $\leqslant \lambda \leqslant$ 2.3775 μm. As expected, the lowest value of χ^2_ν is at [C/Fe] = 0.0. Moving by $\pm$0.1 in the carbon abundance changes the value of χ^2 by two. Thus, the error bar on [C/Fe] is about $\pm$0.05, half that of the error in [Fe/H]. If we limit our analysis to just the CO region itself, 2.2825 μm $\leqslant \lambda \leqslant$ 2.3775 μm (right-hand panel in Figure 2), the result is even tighter, where a change of $\pm$0.1 in the carbon abundance leads to differences in χ^2 that are greater than 9. In this ideal case, with high S/N data, the error bar on [C/Fe] is $\pm$0.01 (again, assuming that HD 3765 has $T_{\rm eff} = 5000$ K and [Fe/H] = 0.0). The uncertainty in [Fe/H] will dominate the error in [C/Fe] for nearly all objects, except those with extremely low values of [C/Fe]. It is important to note that the [C/Fe] values tabulated in H16 and Harrison & Hamilton (2015) are technically [^{12}C/Fe], as those papers assumed $^{12}C/^{13}C = 89$. If the isotopic ratio were smaller than this, the true value of [C/Fe] would be slightly underestimated.

The next result we derive is the error bar for atomic features. Here, we attempt to derive the abundance of sodium using the strong Na I doublets in the *K*-band for analysis. For this test, we will use HD 10476 (K1V), which has nominal values of $T_{\rm eff} = 5189 \pm 53$ K and [Fe/H] $= -0.06 \pm 0.06$. The analysis in H16 found values of $T_{\rm eff} = 5250$ K and [Fe/H] $= -0.20$ for this star. We constructed a grid of models spanning the range 5000 K $\leqslant T_{\rm eff} \leqslant$ 5500 K, and $-0.40 \leqslant$ [Fe/H] $\leqslant 0.25$. Heat maps of the χ^2 results are presented in Figure 3. The leftmost panel in this figure is for the wavelength range 2.08 to 2.14 μm, the middle panel is for 2.19 to 2.29 μm, and the rightmost panel is for 2.21 to 2.29 μm. The white cross delineates the lowest value of χ^2_ν. These wavelength intervals were chosen to avoid H I Br γ (the data reduction process corrupts the spectral regions associated with H I lines) and the CO region. This analysis derives the same result as in H16. Inclusion of the strong Na I feature (at 2.20 μm) in the derivation of [Fe/H] (middle panel) leads to an error bar of $\pm$0.05 on [Fe/H]; however, the mean of the previously published values suggest a slightly higher metallicity than found here. This was the trend found in H16: the derived metallicities for the K-dwarf templates using *IJHK* spectra were slightly lower ($\langle\Delta$[Fe/H]$\rangle = -0.11$) than the means from the literature.

Given these results, we fix the model temperature and [Fe/H] to the values we derived and construct a grid with a range in sodium abundance. In Figure 4, we plot the χ^2_ν values for the

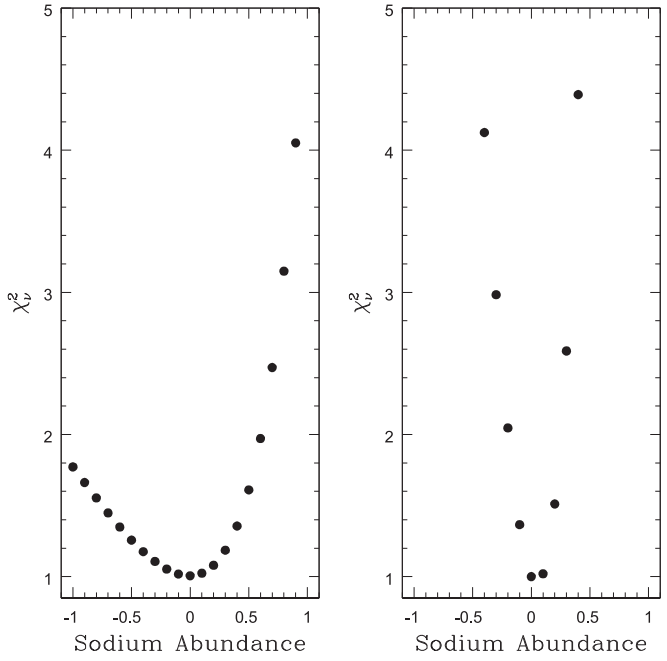

Figure 4. Values of χ^2_ν for different values of the sodium abundance, covering the range $-1.0 \leqslant$ [Na/Fe] $\leqslant +1.0$ for HD 10476. The left-hand panel is for the Na I doublet at 2.2 μm, while the right-hand panel is for the doublet at 2.34 μm.

Na I doublet at 2.20 μm (left-hand panel) and that at 2.34 μm (right-hand panel). For both doublets, the error bar is $\pm$0.15 on [Na/Fe]. With additional Na I doublets to model at 0.82, 1.15, and 1.64 μm, the error bar on [Na/Fe] can drop to levels similar to that for [Fe/H]. It is important to note, however, that it is rare for all five of these doublets to be used in deriving [Na/Fe] for CVs, as the *H*-band can have H I emission near 1.64 μm, the doublet at 1.15 μm is close to a nasty telluric feature, and that at 0.82 μm can often be diluted by emission from the white dwarf and accretion disk. For species with a single strong line, the typical error bar on its abundance will be of order $\pm$0.15 (for these lower-resolution SPEX data). Obviously, like carbon, the final precision for any element rests on the error bars for [Fe/H]. We will use the type of analysis just described in the following to derive error bars on the abundances of ^{13}C, magnesium, and sodium for each of the program objects.

4. Results

The feasibility of using the $^{13}CO_{(2,0)}$ bandhead (λ2.345 μm) to measure the $^{12}C/^{13}C$ ratio was questioned by Dhillon et al. (2002) who noted that there is a Ti I line in the spectra of cool stars located at the same position as this bandhead. They believed that the stronger-than-expected Na I doublet at 2.337 μm indicated that the donor in SS Cyg was covered with starspots and, if true, the Ti I lines would strongly contaminate the $^{13}CO_{(2,0)}$ feature. They suggested a better test would be to use the $^{13}CO_{(4,2)}$ bandhead at 2.403 μm. To illustrate the problem, we present the GNIRS spectrum of AE Aqr in Figure 1 and compare it to models with no carbon. The top spectrum in this figure is a model with solar abundance, $\log g = 4.5$, and $T_{\rm eff} = 5000$ K; the spectrum immediately below this is the same, except with $T_{\rm eff} = 4000$ K. As noted by Dhillon et al., the Ti I line is highly temperature sensitive and increases in strength with decreasing temperature for K dwarfs.

If starspots were to cover a sufficient fraction of the surface so as to result in anomalously strong Ti I absorption, the best-fit spectral model for that object would have a lower temperature. Ti I lines are already incorporated into the modeling process, so the combination of the correct temperature and the fit to all of the ^{13}CO features *should* lead to a reliable value of the $^{12}C/^{13}C$ ratio. As we discuss below, the best-fit temperature for AE Aqr is 5000 K. It is clear that the absorption feature at 2.344 μm is stronger in AE Aqr than the model with $T_{\rm eff} = 5000$ K, suggesting a contribution from $^{13}CO_{(2,0)}$. There is also a feature at 2.374 μm that is suggestive of the $^{13}CO_{(3,1)}$ bandhead. There is no evidence for the $^{13}CO_{(4,2)}$ bandhead at 2.4030 μm. Unfortunately, the $^{13}CO_{(4,2)}$ feature falls in the middle of a weak Na I doublet (at wavelengths of 2.4029 and 2.4043 μm). As we derive below and can be seen in Figure 1, the sodium abundance of AE Aqr appears to be enhanced. We will find that sodium is also super-solar in RU Peg and SS Cyg. Thus, derivation of the $^{12}C/^{13}C$ ratio will be problematic, almost solely resting on the $^{13}CO_{(2,0)}$ feature for our three CVs. It is clear that an enhancement in sodium was the source of the original confusion about the strength of the $^{13}CO_{(2,0)}$ bandhead in SS Cyg.

4.1. AE Aquarii

H16 presented abundance modeling results for AE Aqr derived from lower-resolution *IJHK* spectra obtained with SPEX on the IRTF. They found $T_{\rm eff} = 4750$ K, [Fe/H] = 0.0, and [C/Fe] = -1.0. To limit the parameter space needed to search for the best-fit results for a large number of CVs, only models with $\log g = 4.5$, the value found for field K dwarfs, were run in H16. Given that the orbital period of AE Aqr is $P_{\rm orb} = 9.88$ hr, with component masses of $M_1 = 0.63\ M_\odot$ and $M_2 = 0.37\ M_\odot$ (Echevarría et al. 2008), the surface gravity of the secondary star in AE Aqr should be $\log g \simeq 4.2$. With the rather tight limits derived in H16 for the properties of the donor, we allowed for the possibility that this object might have a lower gravity. Thus, a grid of models with both $\log g = 4.5$ and 4.0 were run covering this parameter space: $4500\ {\rm K} \leqslant T_{\rm eff} \leqslant 5250$ K, $-0.25 \leqslant$ [Fe/H] $\leqslant 0.5$, $-2.0 \leqslant$ [C/Fe] $\leqslant -0.5$, and $4 \leqslant {}^{12}C/{}^{13}C \leqslant 89$.

For both the $\log g = 4.5$ ("dwarf model") and the $\log g = 4.0$ ("subgiant model"), the temperature and [Fe/H] are poorly constrained due to the limited wavelength coverage of the GNIRS data and the unusual abundances of carbon and sodium in AE Aqr. For the dwarf model, using the spectral region $\lambda < 2.290$ μm, we derive $T_{\rm eff} = 5000 \pm 250$ K and [Fe/H] = 0.00 ± 0.20. These are essentially consistent with the values found in H16, and we adopt the newly derived values in the following. Given the spectral resolution of this GNIRS data, we derived an independent measurement of $v\sin i$ for AE Aqr. Echevarría et al. (2008) found that the value of $v\sin i$ was dependent on the orbital phase. Near $\phi = 0$, they found $v\sin i = 92\ {\rm km\ s^{-1}}$, while at $\phi = 0.25$, $v \sin i = 114\ {\rm km\ s^{-1}}$. To derive a new estimate of $v\sin i$, we generated a series of models (using the parameters $T_{\rm eff} = 5000$ K, $\log g = 4.5$) and velocity broadened them using the program *a v sin i* by Gray.[3] We then performed a χ^2 minimization analysis using the Ca I triplet lines at 1.28 μm and the Mg I line at 2.29 μm. We found a best-fit value of $110 \pm 11\ {\rm km\ s^{-1}}$ for our data, where the mean phase was $\langle\phi\rangle = 0.15$. We broaden our model spectra using this value.

[3] http://www.appstate.edu/~grayro/spectrum/spectrum276/node31.html

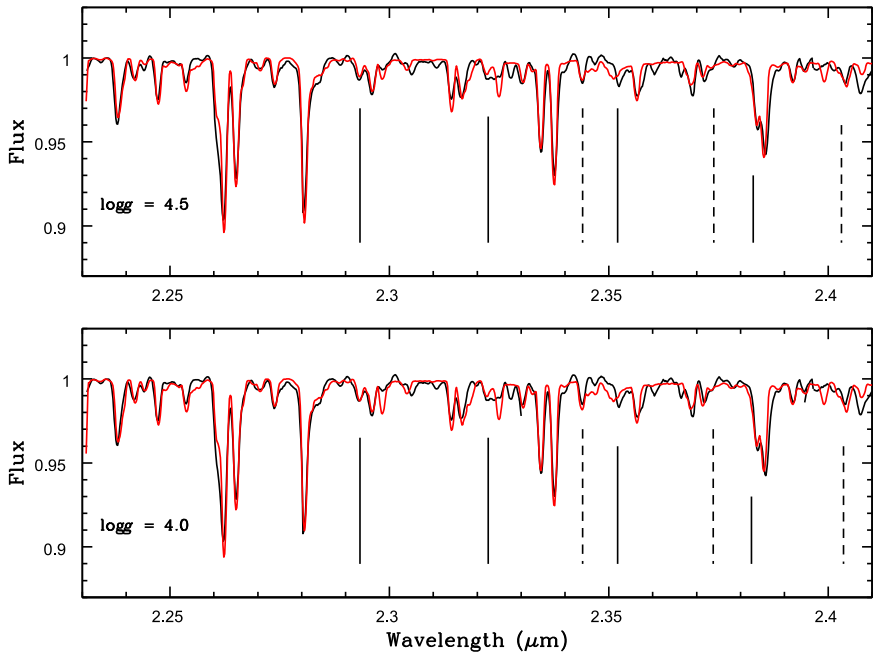

Figure 5. GNIRS spectrum of AE Aqr (black) compared to the log$g = 4.5$ (top panel) and the log$g = 4.0$ (bottom panel) models (red), described in the text. The positions of the strongest ^{12}CO bandheads are marked by solid vertical lines, and those of ^{13}CO by dashed lines.

This same program, *av*sin*i*, was used to produce velocity-broadened model spectra for all three objects in this paper.

As noted above, a Na I doublet could affect the $^{13}CO_{(4,2)}$ bandhead, so first we derive the sodium abundance. We ran a grid of models where we changed the abundance of sodium over the range $0.0 \leqslant [Na/Fe] \leqslant 1.0$. The best-fit model has $[Na/Fe] = +0.5 \pm 0.05$, three times the solar abundance of this element. As noted in H16, the carbon abundance in AE Aqr is very low. They derived $[C/Fe] = -1.0$ using lower-resolution SPEX/IRTF data. The higher resolution of the GNIRS data allows for a more precise measurement: $[C/Fe] = -1.40 \pm 0.05$.

At this low of an abundance, the ^{13}CO features will be difficult to distinguish. Even if the CN cycle had run to completion, the $^{13}CO_{(2,0)}$ feature would be one-quarter the strength of the $^{12}CO_{(2,0)}$ bandhead. Given that the depth of the $^{12}CO_{(2,0)}$ feature is only about 1.5% below the continuum, it will be difficult to isolate the contribution of the $^{13}CO_{(2,0)}$ bandhead. In Figure 5, we overlay the best-fitting model with the derived values of sodium and carbon, and with $^{12}C/^{13}C = 4$.

Tests using just the $^{13}CO_{(2,0)}$ bandhead indicate that low values of the isotopic ratio are preferred, $^{12}C/^{13}C = 5 \pm 2$ (see Figure 6). However, the structure in the continuum of AE Aqr at this wavelength is quite different from the model, and given that the Ti I feature appears to be of similar strength to the $^{13}CO_{(2,0)}$ bandhead, this derivation is not especially robust.

For the (log$g = 4.0$) subgiant model, we found best-fitting values of $T_{\rm eff} = 4750 \pm 250$ K and $[Fe/H] = 0.0 \pm 0.20$. We will fix these values when estimating the abundances of other species. A χ^2 analysis for the carbon abundance finds $[C/Fe] = -1.70 \pm 0.08$, and for sodium we derive $[Na/Fe] = +0.52 \pm 0.06$. Again, we were not able to adequately constrain the $^{12}C/^{13}C$ ratio. A model spectrum with these parameters, and $^{12}C/^{13}C = 4$, is overlaid on the GNIRS data for AE Aqr in Figure 5.

With the limited wavelength coverage of the GNIRS spectra, we cannot decide between either gravities. To attempt this, we return to the *IJHK* spectrum obtained using SPEX at the IRTF. As noted in H16, the resolution of the SPEX data is generally insufficient for discrimination between dwarfs and subgiants.

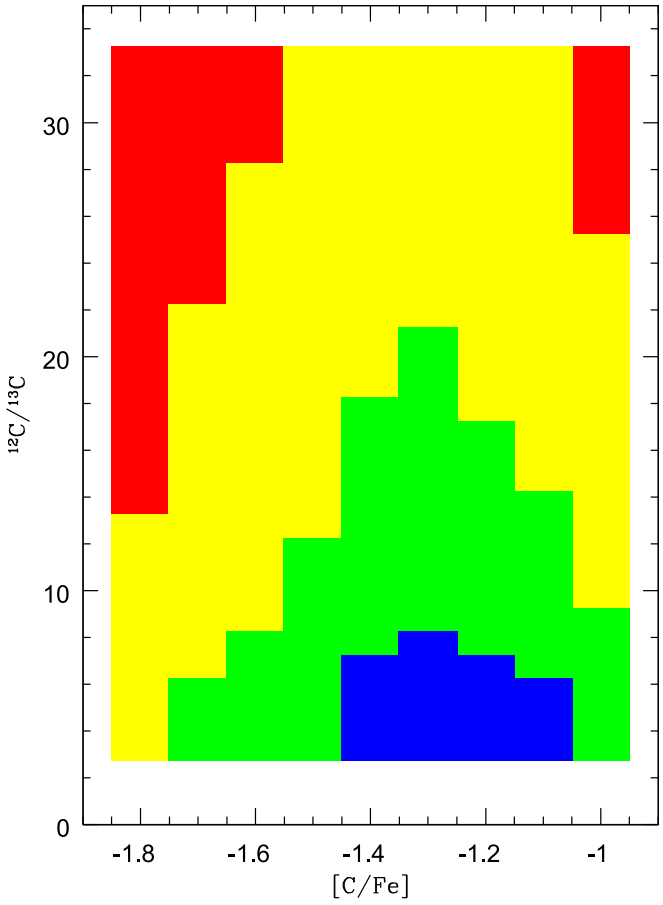

Figure 6. Heat map of the χ^2 analysis (log$g = 4.5$) for just the $^{13}CO_{(2,0)}$ bandhead of AE Aqr. The $^{12}C/^{13}C$ ratio appears to be low, but given that the derived carbon abundance of $[C/Fe] = -1.4$, it cannot be tightly constrained.

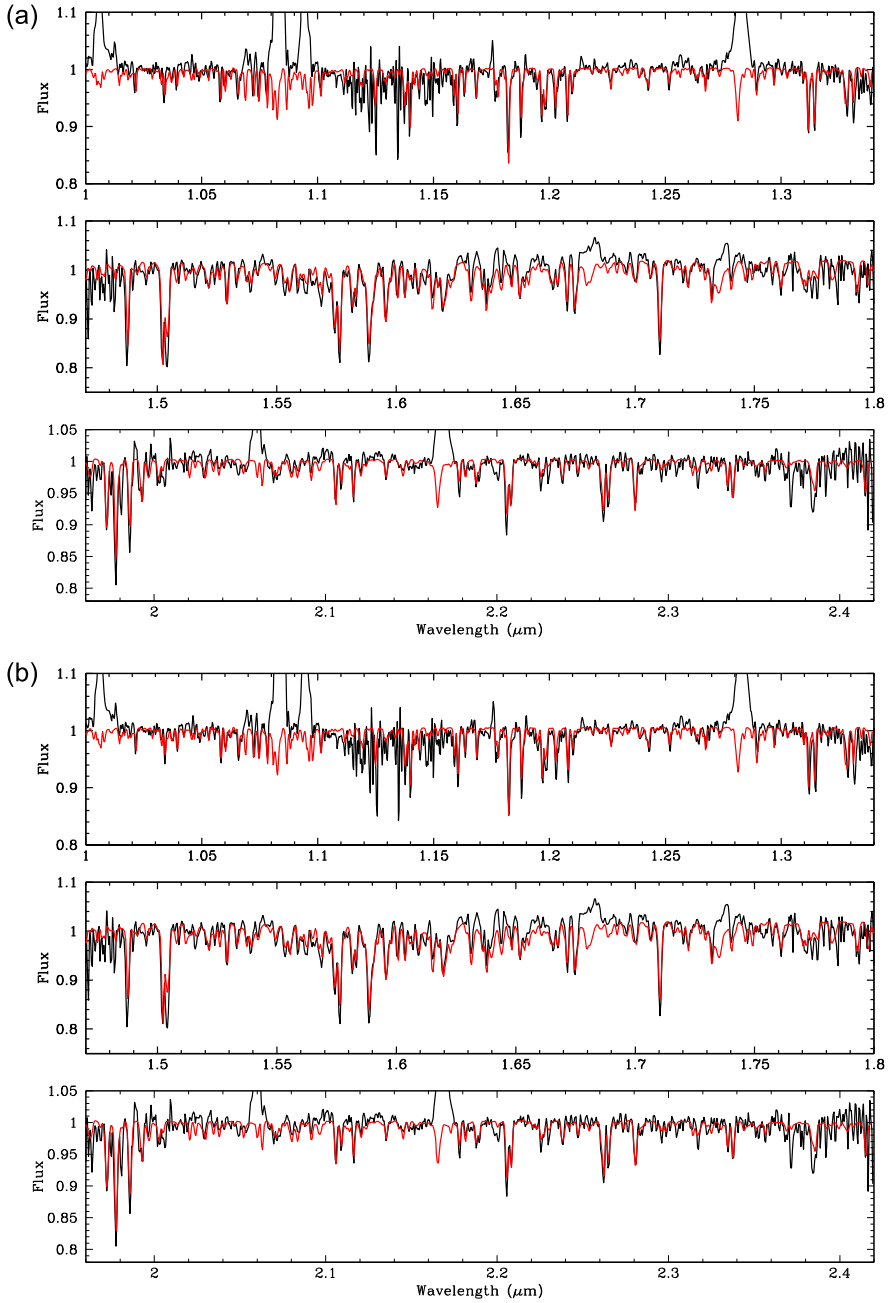

Figure 7. (a) Comparison of the best-fit log $g = 4.5$ model (red) using the parameters derived using the GNIRS data for AE Aqr overlaid on the *JHK* portion of the SPEX data (black). We have adjusted the limits on this plot to allow for a better inspection of the fit of the model to the data. See H16 for the full data set with the vertical range set so as to include the strong emission line features. (b) Same as 7a, but for log$g = 4.0$.

We compare models using the parameters above in Figure 7. Given the temperature ambiguity, for the χ^2 tests we constructed a grid of four models using the abundances listed above, but for both temperatures at both gravities. We find that the dwarf model with $T_{\rm eff} = 5000$ K fits better in the *J*- and *K*-bands, while a subgiant model with $T_{\rm eff} = 5000$ K fits better in the *H*-band (the wavelength interval used for the χ^2 tests in the *J*-band was $1.155 \leqslant \lambda \leqslant 1.27\,\mu$m, for *H* it was $1.5 \leqslant \lambda \leqslant 1.63\,\mu$m, and for *K* it was $2.19 \leqslant \lambda \leqslant 2.36\,\mu$m). While $T_{\rm eff} = 5000$ K is clearly the best fit for temperature, we cannot constrain the gravity. We can, however, state with confidence that no matter the gravity, the donor star in AE Aqr suffers an extreme carbon deficit and has a sodium abundance that is three times the solar value.

4.2. RU Pegasi

H16 found that analysis of Keck NIRSPEC and IRTF SPEX data resulted in a model for the donor star ($\log g = 4.5$) with these parameters: $T_{\rm eff} = 5000$ K, [Fe/H] $= -0.3$, [C/Fe] $= -0.4$, and [Mg/Fe] -0.14. They also noted that the donor star in RU Peg is much more luminous than a dwarf of its spectral type and is probably a subgiant. The GNIRS spectrum of RU Peg presented in Figure 8 is odd, with emission peaks that precede the ^{12}CO bandheads and CO absorption features that

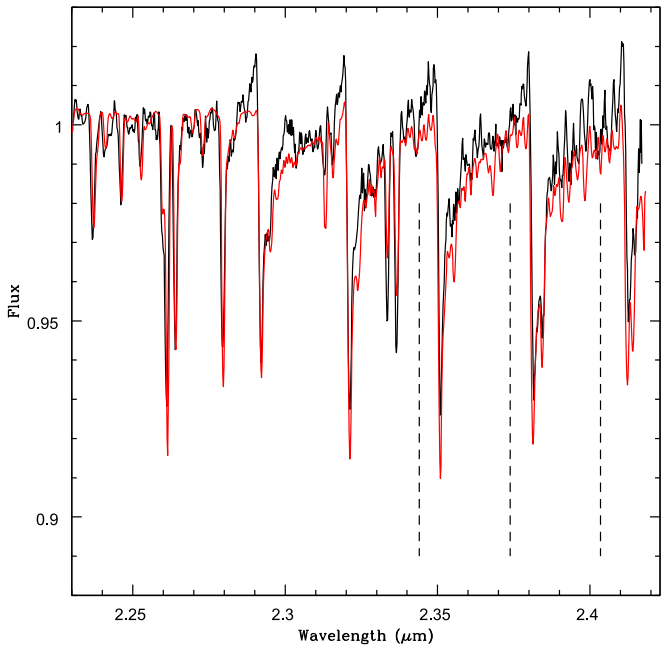

Figure 8. GNIRS data for RU Peg (black), compared to the synthetic spectrum (with $\log g = 4.5$) with the parameters listed in the text (red).

are narrower than expected. As discussed in H16, this is the telltale sign of CO emission. Such features have not been seen in any of our previous three epochs of *K*-band spectroscopy of RU Peg. At the time of these observations, the system was halfway between two outbursts. Obviously, the presence of CO emission features hampers our ability to independently examine the abundance of carbon and its isotopes. It does appear, however, that all three of the strongest ^{13}CO bandheads are present in this spectrum.

We return to the IRTF SPEX data used in H16 to construct baseline models. For $\log g = 4.5$, χ^2 analysis using a grid of models (with $v \sin i = 95\ \mathrm{km\ s^{-1}}$; H16) that spanned the full range in temperature ($4000\ \mathrm{K} \leqslant T_{\rm eff} \leqslant 5500\ \mathrm{K}$) and metallicity ($-1.0 \leqslant [\mathrm{Fe/H}] \leqslant 0.5$) finds results similar to H16: $T_{\rm eff} = 5125 \pm 144$ and $[\mathrm{Fe/H}] = -0.28 \pm 0.10$. Four wavelength intervals were used in deriving this result: 1.115 to 1.220 μm, 1.560 to 1.162 μm, 2.08 to 2.13 μm, and 2.19 to 2.288 μm. In the *J*-band, H16 used the wavelength interval 1.16 to 1.26 μm. As can be seen in their Figure 1(b), by far the strongest line in this bandpass is Mg I at 1.182 μm. As found in H16 and quantified below, magnesium has a subsolar abundance in the donor star of RU Peg. As shown in Figure 9, this line appears to be strong enough to skew the final value of the metallicity in this bandpass. The two bandpasses in the *K*-band also have have Mg I lines, but they are not as dominant as that in the *J*-band. For $\log g = 4.0$, the effect of the Mg I line at 1.18 μm is even larger and forces the answer to a much lower metallicity than found in the other wavebands. Excluding the result from the *J*-band χ^2 analysis, we find $T_{\rm eff} = 4750 \pm 110$ K and $[\mathrm{Fe/H}] = -0.2 \pm 0.1$. Including this result, we find $T_{\rm eff} = 4812 \pm 125$ K and $[\mathrm{Fe/H}] = -0.28 \pm 0.17$. The χ^2 analysis for these four bandpasses, and $\log g = 4.0$, is plotted in the bottom row of Figure 9. To derive elemental abundances for the "subgiant" models, we will use $T_{\rm eff} = 4750$ K and $[\mathrm{Fe/H}] = -0.2$.

To constrain the magnesium abundance, we focus on four isolated spectral lines at 1.182, 1.486, 1.711, and 2.282 μm. For the $\log g = 4.5$ ("dwarf") model, we find $[\mathrm{Mg/Fe}] = -0.20 \pm 0.08$, and for the subgiant model we derive $[\mathrm{Mg/Fe}] = -0.18 \pm 0.05$. Using the baseline models, we derive the following results for carbon: $[^{12}\mathrm{C/Fe}]_{\rm Dwarf} = -0.20 \pm 0.03$ and $[^{12}\mathrm{C/Fe}]_{\rm Subgiant} = -0.60 \pm 0.03$. We overlay the dwarf model with these parameters on the GNIRS data in Figure 8. Even with the excesses due to CO emission, it is clear that the sodium doublet at 2.34 μm is stronger in RU Peg than in the model. We again analyze the IRTF SPEX data to estimate a value for the sodium enhancement. Using the two doublets in the *K*-band, we find $[\mathrm{Na/Fe}] = 0.5 \pm 0.15$ for the dwarf model, and $[\mathrm{Na/Fe}] = 0.3 \pm 0.18$ for the subgiant model. The χ^2 analysis for all three elements, and for both gravities, is presented in Figure 10.

Given that we have confidence in the underlying model, we can subtract the donor star contribution to attempt to quantify the CO emission line profiles. The result of this process is shown in the top panel of Figure 11. We have generated a CO emission spectrum, velocity broadened to 700 km s^{-1}, and plot it in green. This is a larger velocity width than either the H I or He I emission lines seen in the SPEX data for RU Peg (FWHM $\sim 600\ \mathrm{km\ s^{-1}}$). The result of subtracting off the CO emission spectrum from the GNIRS data is shown in the bottom panel of Figure 11, where the result is compared to our best-fitting dwarf model.

The fit to the CO-subtracted spectrum by the dwarf model is quite reasonable, and we use this spectrum to derive limits on the ^{12}C/^{13}C ratio. We will rely only on the $^{13}\mathrm{CO}_{(2,0)}$ bandhead, since, as we note above, the $^{13}\mathrm{CO}_{(4,2)}$ feature is convolved with a Na I doublet, while the subtraction of the CO emission spectrum appears to have corrupted the profile of the $^{13}\mathrm{CO}_{(3,1)}$ bandhead. The joint χ^2 analysis for the ^{12}CO ($2.2895\ \mu\mathrm{m} \leqslant \lambda \leqslant 2.3292\ \mu$m) and ^{13}CO ($2.3420\ \mu\mathrm{m} \leqslant \lambda \leqslant 2.3452\ \mu$m) regions for both the dwarf and subgiant models is presented in Figure 12. For $\log g = 4.5$, the minimum in the combined χ^2 falls at $[\mathrm{C/Fe}] = -0.2$, and $^{12}\mathrm{C}/^{13}\mathrm{C} = 15$. The minimum for ^{12}CO for these models occurs at $[\mathrm{C/Fe}] = -0.2$ and has $^{12}\mathrm{C}/^{13}\mathrm{C} = 89$, while the minimum for ^{13}CO has $[\mathrm{C/Fe}] = -0.2$ and $^{12}\mathrm{C}/^{13}\mathrm{C} = 10$. The difference between the ^{12}CO minimum and the combined minimum is $\Delta\chi^2_{\rm nu} = 2.75$. The minimum in ^{13}CO has $\Delta\chi^2_{\rm nu} = 0.90$ from the joint-fit result. The absolute carbon abundance we find for the donor star in RU Peg from the CO-subtracted GNIRS spectrum is in agreement with that from the SPEX data, helping to validate the process used to arrive at these results. Obviously, the $^{12}\mathrm{C}/^{13}\mathrm{C}$ ratio is not small enough to alter the ^{12}C abundance sufficiently for it to create a detectable difference from models with cosmic values for the isotopic ratio.

Like the results for the dwarf model, the combined χ^2 analysis for the subgiant model finds a global carbon abundance identical to that derived from the IRTF data set: $[\mathrm{C/Fe}] = -0.6$. For the subgiant model, the isotopic ratio is slightly lower than that for the dwarf: $^{12}\mathrm{C}/^{13}\mathrm{C} = 6$. The best-fitting ^{12}CO model has $[\mathrm{C/Fe}] = -0.6$, and $^{12}\mathrm{C}/^{13}\mathrm{C} = 27$. The difference between the ^{12}CO minimum and the joint-fit minimum is $\Delta\chi^2_{\rm nu} = 3.5$, while for ^{13}CO this difference is $\Delta\chi^2_{\rm nu} = 2.6$, with the preferred model for ^{13}CO having $[\mathrm{C/Fe}] = -0.4$, and $^{12}\mathrm{C}/^{13}\mathrm{C} = 32$. The best combined-fit model for $\log g = 4.0$ strengthens the case for a low isotopic ratio of carbon in the donor of RU Peg.

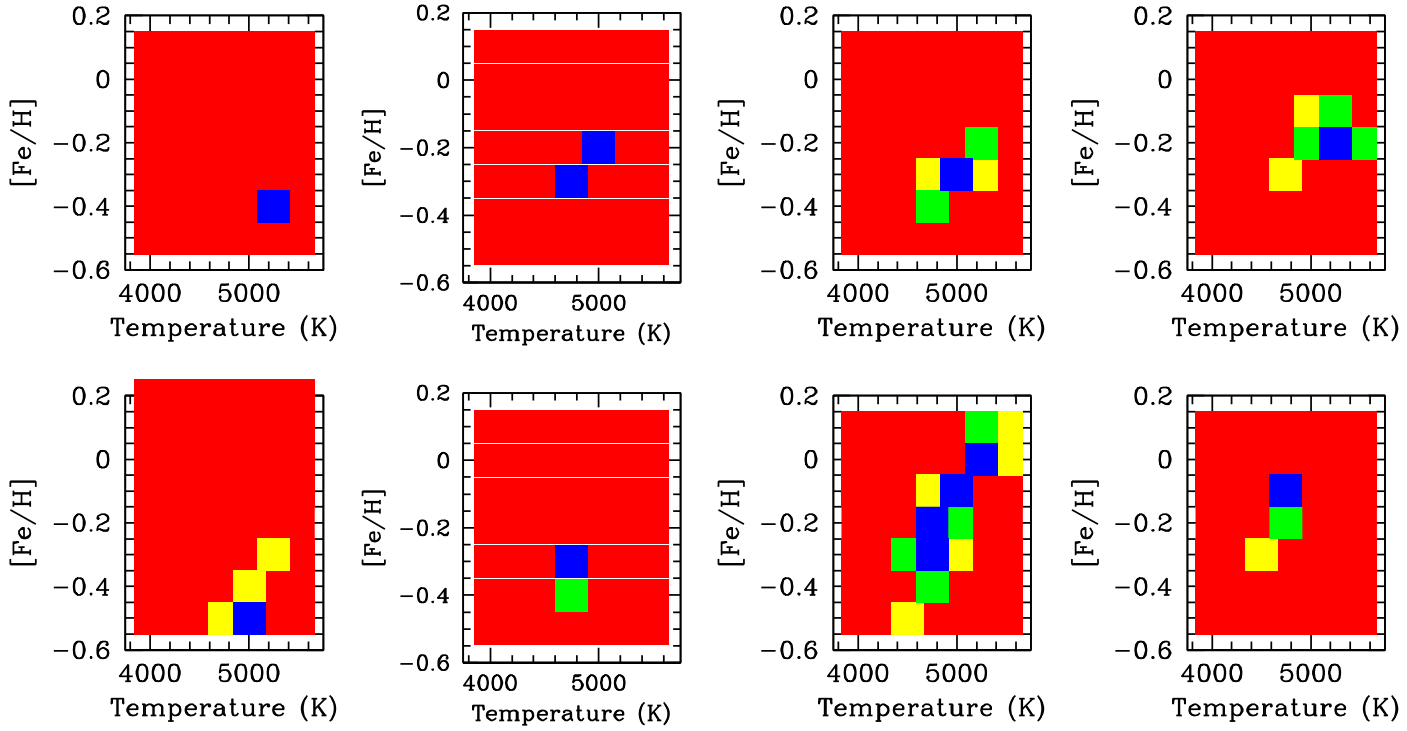

Figure 9. χ^2 analysis for the IRTF SPEX data for RU Peg. The top row is for log$g$ = 4.5, and the bottom row is for log$g$ = 4.0. The leftmost panels are the results for the J-band region, the next panels over are for the H-band, and the rightmost panels are for the two wavelength regimes in the K-band.

4.3. SS Cygni

H16 presented analysis of IRTF SPEX and Keck NIRSPEC data for SS Cyg and found a subsolar metallicity, and deficits of both carbon and magnesium. Unfortunately, the GNIRS observations occurred during an outburst of SS Cygni. Thus, these new data for SS Cyg are not amenable to analysis without assuming an abundance pattern due to the uncertain level of contamination from the white dwarf and accretion disk. At the time of the second epoch of GNIRS observations, SS Cyg was roughly 3 mag fainter than the standard star ($K_{\rm HD209932} = 6.6$) in this bandpass. Szkody (1977) found that the K magnitude of SS Cyg at this point in its outburst is $K \sim 9.0$. This should be compared to the mean value at minimum of $\langle K \rangle = 9.45$. Unless SS Cyg has a peculiar post-outburst spectral energy distribution, the contamination should not be very large. This is confirmed by the spectra: we find that we needed to dilute a synthetic spectrum generated using the parameters in H16 by a factor of 1.6 to match the GNIRS observations. Before we can attempt to measure the ^{12}C/^{13}C ratio in the GNIRS spectrum of SS Cyg, we need to be confident of the metallicity and elemental abundances of its donor star.

H16 found that both carbon and magnesium are deficient in the donor star of SS Cyg. We show below that the abundance of sodium is also enhanced. Thus, the derivation of [Fe/H] in H16 might be suspect given that the spectral features from these elements are among the strongest in the near-IR spectra of K dwarfs. We performed a χ^2 analysis using the IRTF SPEX data discussed in H16. Models covering the full temperature and metallicity range were constructed. As in the analysis for RU Peg, inclusion of the Mg I line at 1.182 μm skews the best-fitting model for the J-band, giving $T_{\rm eff} = 5250$ K and [Fe/H] = −0.40. Excluding this line, we find $T_{\rm eff} = 5000$ K and [Fe/H] = −0.20. The final results of the χ^2 analysis for SS Cyg using the SPEX data in all three bandpasses is identical to that in H16: $T_{\rm eff} = 4750 \pm 204$ K and [Fe/H] = −0.30 ± 0.15. These values will form the basis for the analysis that follows.

For the derivation of the carbon, magnesium, and sodium abundances, we again use the IRTF spectrum. Given the strength of the CO features in the donor star of SS Cyg, the χ^2 analysis, Figure 13, delivers a very tight constraint for carbon: [^{12}C/Fe] = −0.20 ± 0.01. As noted earlier, the error bar on [Fe/H] dominates the uncertainty in the carbon abundance. To derive the magnesium abundance, we use the same four spectral lines as used in RU Peg. The χ^2 results for all four lines are presented in Figure 13. The derived magnesium abundance for the J-band line is much lower, [Mg/Fe] = −0.9, than that found from the other three lines, [Mg/Fe] = −0.40 ± 0.1. This is almost certainly due to contamination from an unidentified emission feature very near the 1.182 μm Mg I line that is often visible in CVs with hot/luminous accretion disks (e.g., LS Peg; see Figure 18 in H16). Finally, we derive the abundance of sodium. For this we use the two doublets in the K-band, as the doublet near 1.15 μm is corrupted by the telluric absorption. The χ^2 analysis for the two doublets of sodium are shown separately in Figure 13. The final result for its abundance is [Na/Fe] = +0.40 ± 0.12.

The GNIRS spectrum of SS Cyg is plotted in Figure 14 along with a model with $T_{\rm eff} = 4750$ K, $v \sin i = 89$ km s^{-1} (Bitner et al. 2007), [Fe/H] = −0.3, [C/Fe] = −0.2, [Mg/Fe] = −0.4, [Na/Fe] = +0.4, and ^{12}C/^{13}C = 89. Even given the unusual continuum, the ^{13}CO$_{(2,0)}$ bandhead is prominent. It is also clear from this spectrum that there is contamination of the CO bandheads by excess emission, as they are narrower than expected, with strong deviations in the red wings of the features. Unlike RU Peg, there is no blue wing on the CO absorption features that would confirm this as CO emission. Since SS Cyg was in outburst, the observed excess might be due to hydrogen

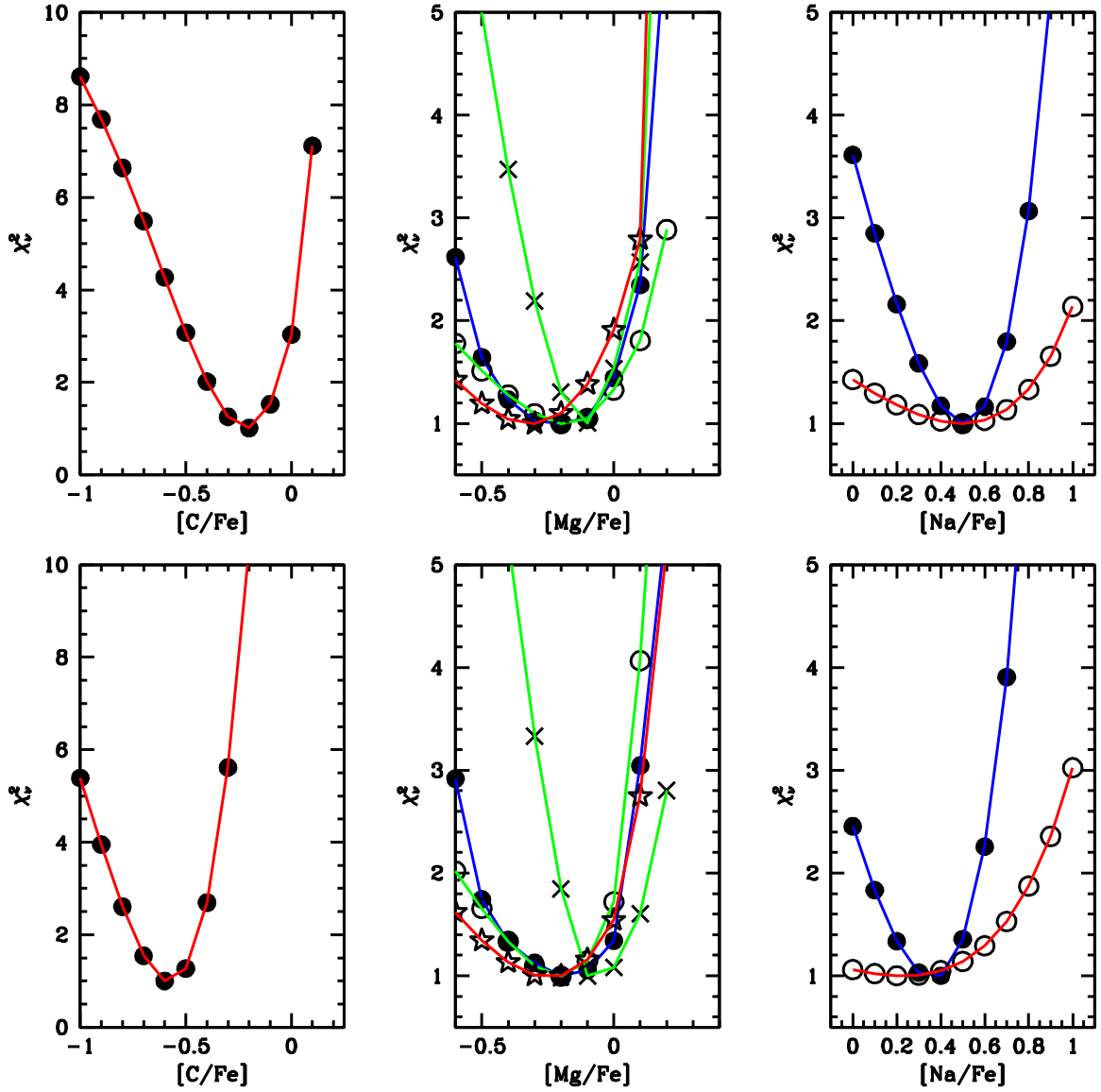

Figure 10. χ^2 analysis for the IRTF SPEX spectrum of RU Peg. In the left-hand panels are the result for carbon. The middle panels plot the χ^2_ν values for the four lines of Mg I (blue is the *J*-band, green is the *H*-band, and red is the *K*-band). The right-hand panels plot the analysis for the two Na I doublets in the *K*-band (blue is the doublet at 2.20 μm and red is that at 2.34 μm). The top row is for log$g = 4.5$, and the bottom row is for log$g = 4.0$.

emission. We have marked the location of the H I Pfund lines in Figure 14. As discussed in Kromer et al. (2007 and references therein), during the decline of SS Cyg from outburst, its spectrum transitions from one with H I in absorption to one with H I in emission. Hessman (1986) found that SS Cyg also has strong He II λ4686 Å emission during the decline from outburst. There are He II emission lines in this bandpass at 2.314 μm, 2.347 μm, and 2.379 μm (seen in the spectra of Wolf–Rayet stars; Figer et al. 1997). These are also marked in the top panel of Figure 14. Neither hydrogen nor helium emission provide a viable explanation for the excess in the red wings of the CO bandheads.

If we subtract the model spectrum from the observed data, we get the spectrum plotted in the middle panel of Figure 14. For comparison, a CO emission spectrum, broadened to 700 km s^{-1}, is plotted in this same panel. It is clear that the excess observed in SS Cyg is due to CO emission, but it is *redshifted*. The offset of the observed peaks from the model spectrum corresponds to a velocity of 300 km s^{-1}. Note that the radial velocity of the secondary star at the phase of the GNIRS observations was $K_2 \sim +160$ km s^{-1} (Bitner et al. 2007) and has been removed from our our data set. This suggests that the CO emission, if its origin is in the accretion disk, is much stronger on the receding side of the accretion disk, and must be located somewhere between the primary and secondary stars.

Subtracting a redshifted and normalized CO emission spectrum from the GNIRS data, we can attempt to derive the $^{12}C/^{13}C$ ratio. As we did for RU Peg, we only use the $^{13}CO_{(2,0)}$ bandhead. As shown in Figure 15, a combined χ^2 analysis finds the best-fitting values of [C/Fe] $= -0.1$ and $^{12}C/^{13}C = 4$. From the IRTF data, we derived a value of [^{12}C/Fe] $= -0.2$. At this abundance, values within the 1σ error bar in χ^2 only occur for $^{12}C/^{13}C > 32$. The combined-fit value is 2σ away from the ^{12}CO result. The $^{13}CO_{(2,0)}$ feature in SS Cyg is very strong, and at [C/Fe] $= -0.1$, only the most extreme value of $^{12}C/^{13}C$ fits the observations. The minimum in the χ^2 values of the isotopic ratio occurs at 76 for [C/Fe] $= +0.2$, 18 for [C/Fe] $= +0.1$, and 9 for [C/Fe] $= +0.0$. However, such values for the global carbon abundance are excluded. The error

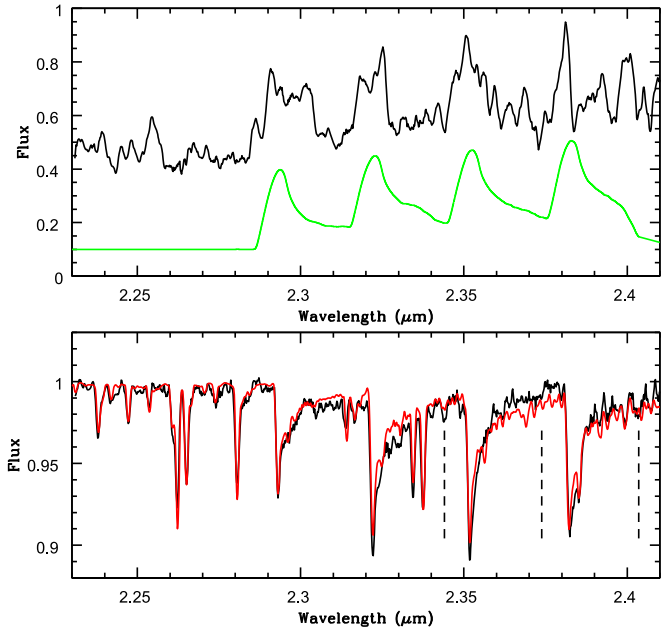

Figure 11. In the top panel is the result of subtracting the best-fitting synthetic (dwarf) spectrum for RU Peg from the GNIRS data (black). This spectrum has been boxcar smoothed by 10 pix. We plot a model CO emission spectrum (green) that has been Gaussian broadened to 700 km s^{-1}. In the bottom panel, we plot the result of subtracting the model CO spectrum from the GNIRS data and compare it to the best-fit dwarf model. Note that the dwarf model has $^{12}C/^{13}C = 89$.

on $^{12}C/^{13}C$ at [C/Fe] $= -0.1$ appears to be very small, as by [C/Fe] $= -0.2$ the best fit for the ^{13}CO feature is at $^{12}C/^{13}C = 5$, but has $\Delta\chi^2_\nu = 280$! A value of $^{12}C/^{13}C = 4$ is equivalent to an increase in the ^{12}C abundance by $+0.1$, and thus our abundance for carbon is consistent with the global value deduced from the IRTF data. While the precision of these measurements appear quite tight, given the fact of dilution due to the outburst *and* the presence of CO emission, the true precision (at least on $^{12}C/^{13}C$) is likely to be poorer than calculated. We compare the final model to the CO-subtracted GNIRS data in Figure 14. While the fit to the $^{13}CO_{(2,0)}$ bandhead is acceptable, the $^{13}CO_{(4,2)}$ absorption is not as strong as predicted by the model. This is almost surely a result of an uncertain telluric/flux correction at the extreme red end of the data set and the CO subtraction process.

5. Summary and Conclusions

Given the uncertainty about the reliability of using the $^{13}CO_{(2,0)}$ bandhead to determine the $^{12}C/^{13}C$ ratio in the donor stars of CVs, we have obtained *K*-band spectra that cover three ^{13}CO features. All three CV secondary stars show evidence for significant enhancements of ^{13}C. More surprising, however, was the derivation of super-solar abundances of sodium in all three objects. Due to a variety of reasons, the results for the isotopic ratio of carbon are not as robust as were initially expected. While the extreme carbon deficit in AE Aqr and the (weak) CO emission in RU Peg and SS Cyg complicated our efforts, the enhanced sodium abundance added additional uncertainty. Normally, the sodium doublet that coincides with the $^{13}CO_{(4,2)}$ bandhead at 2.403 μm is weak enough to not compromise the use of this feature in deriving the isotopic ratio. Here, however, all three CVs have donor stars with large super-solar abundances of this element. The finding of

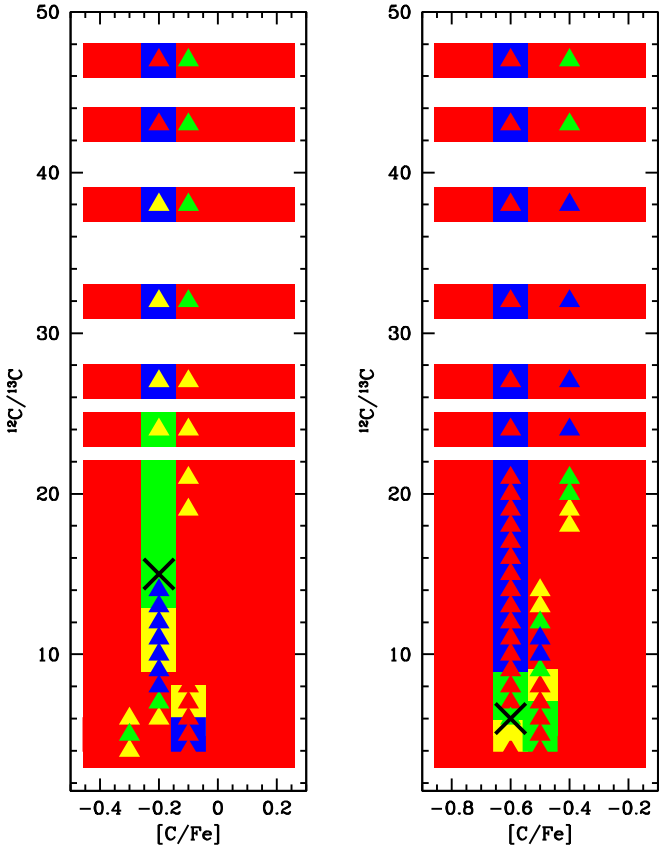

Figure 12. χ^2 analysis for the CO emission-subtracted GNIRS spectrum of RU Peg for log$g = 4.5$ (left) and for log$g = 4.0$ (right). The χ^2_ν values for the fit to ^{12}CO are plotted as filled squares in both panels, while the results for ^{13}CO are plotted as filled triangles. The color coding is blue for $\chi^2_\nu \leqslant 2$, green for $2 < \chi^2_\nu \leqslant 4$, yellow for $4 < \chi^2_\nu \leqslant 7$, and red for $\chi^2_\nu > 7$. A black cross marks the position of the best combined fit. Note that a coarse grid for $^{12}C/^{13}C > 20$ was used for computational efficiency and because it is difficult to discriminate between models with large isotopic ratios.

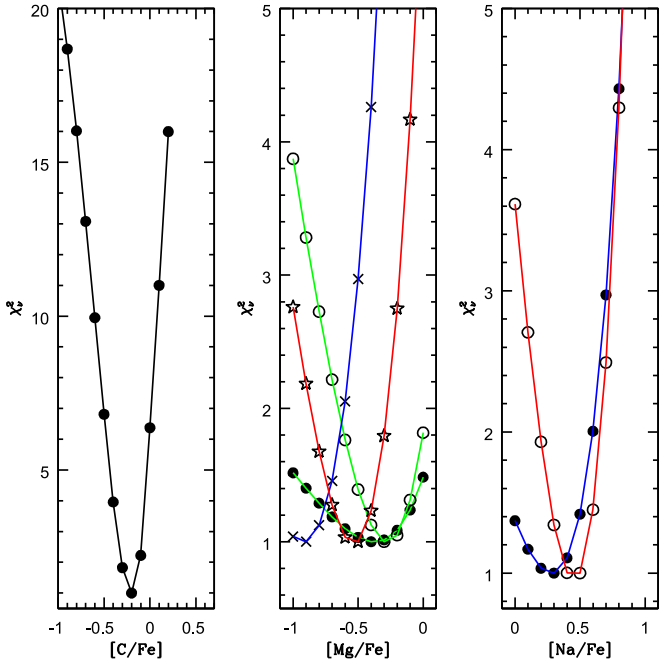

Figure 13. χ^2 analysis for the IRTF SPEX spectrum of SS Cyg as in Figure 10, but only for log$g = 4.5$.

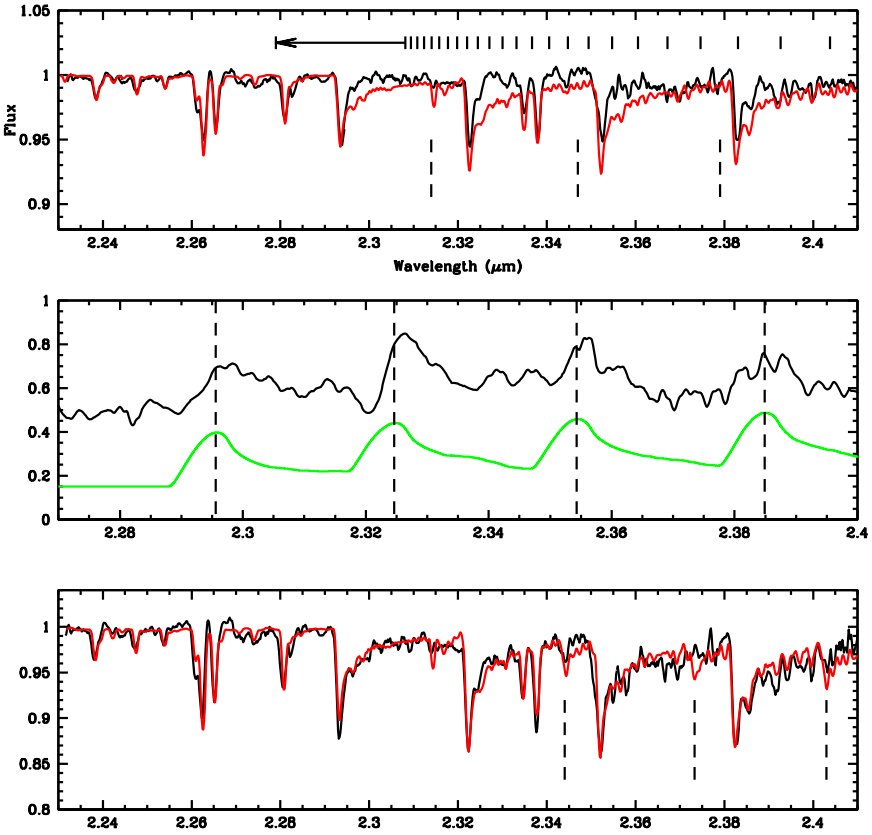

Figure 14. In the top panel is the GNIRS data for SS Cyg (black), compared to the synthetic spectral model described in the text (red). Note that this particular model has $^{12}C/^{13}C = 89$. In this panel, we have also plotted the location of a number of H I Pfund lines that fall in this bandpass (solid vertical line segments with arrow). The H I Pfund continuum limit is at 2.279 μm. We also locate the positions of the three He II lines mentioned in the text (dashed lines). Subtracting the model spectrum from the GNIRS data leads to the spectrum (black) in the center panel (the subtracted spectrum has been boxcar smoothed by 10 pixels). A model CO emission spectrum, velocity broadened to 700 km s^{-1}, is plotted in green. The peaks of the CO emission are located with vertical dashed lines. In the bottom panel, we have subtracted the model CO emission spectrum from the GNIRS data to produce the final spectrum of SS Cyg (black). We overlay the best-fit spectrum (red), having [C/Fe] = −0.1 and $^{12}C/^{13}C = 4$.

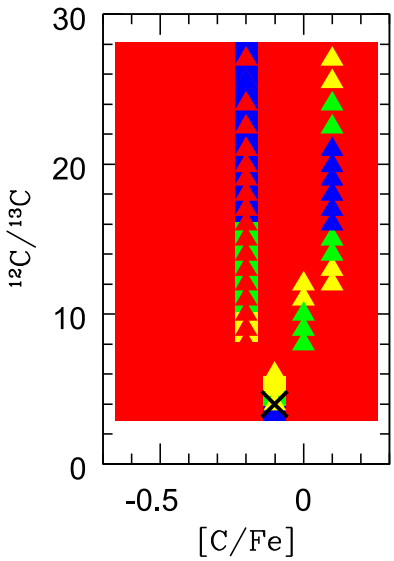

Figure 15. χ^2 analysis for the abundance of carbon and the $^{12}C/^{13}C$ ratio for the donor star of SS Cyg as in Figure 12, but only for log$g = 4.5$ here. The minimum in the combined χ^2 occurs at [C/Fe] = −0.1 and $^{12}C/^{13}C = 4$, and is indicated by the black cross.

enhanced levels of sodium in the donor of SS Cyg does, however, allay some of the fears in using the $^{13}CO_{(2,0)}$ feature for isotopic carbon measurements. While there is a Ti I line located within this bandhead, it is accounted for when generating synthetic spectra. Only a highly discrepant temperature assignment would lead to erroneous measures of $^{12}C/^{13}C$ when using the $^{13}CO_{(2,0)}$ feature.

How do we arrive at donor stars with low abundances of ^{12}C but enhanced levels of ^{13}C? There are two realistic ways to achieve this result: (1) the donor star has undergone significant evolution prior to becoming a CV or (2) the donor has accreted large quantities of CNO processed material during the brief common envelope phase that follows a classical nova eruption. While Marks & Sarna (1998) found that it was possible to dramatically pollute the photosphere of a CV donor following a nova outburst, it seems improbable that the $^{12}C/^{13}C$ ratio could be maintained at such low values for very long. The pre-existing $^{12}C/^{13}C$ ratio in the secondary star, presumably near 89, when combined with the convection found in late-type stars, would quickly drive the value of the ^{13}C enhancement to much lower levels than observed here. In addition, as noted by José & Hernanz (2007), classical nova eruptions on CO white dwarfs typically do not synthesize elements beyond CNO. Thus, odd abundances in magnesium or sodium would require eruptions on ONeMg white dwarfs. The primaries in the three CVs investigated here do not appear to be massive ONeMg white dwarfs. We conclude that significant evolution prior to the semi-contact phase that includes CNO cycle nucleosynthesis, as modeled by Podsiadlowski et al. (2003) and Goliasch & Nelson (2015), is the actual cause of ^{13}C enhancements. In

neither case, however, do those models predict alterations in the sodium or magnesium abundances.

The enhancement of sodium seen in all three objects is puzzling. In H16, we discussed the unusual object QZ Ser, an object where the derived sodium abundance was 33× solar, while simultaneously having an enormous deficit of carbon ([C/Fe] = −1.7). We have found a similar carbon deficit in AE Aqr. QZ Ser is a short period CV (P_{orb} = 2 hr) whose secondary has an anomalously hot spectral type near K4 (Thorstensen et al. 2002; Harrison et al. 2009). Thorstensen et al. conclude that the most likely explanation for such an object is that it is hydrogen deficient. H16 found that they could reproduce the *JHK* spectra of this object with a model that had a significant deficit of hydrogen—30% of the solar value. As they noted, the use of solar abundance pattern atmospheres to derive synthetic spectra in which the hydrogen abundance is non-solar, is problematic.

An enhancement of sodium would appear to require hotter internal temperatures (see Arnould et al. 1999) than is possible for the low-mass donor stars commonly envisioned in population synthesis calculations for CVs. The abundance anomalies that have now been observed include carbon deficits, enhanced levels of ^{13}C, enhancements of nitrogen and sodium, and deficits of magnesium. We do not see abundance differences for iron, calcium, or titanium. For QZ Ser, H16 found an enhancement of aluminum. Aluminum does not appear to be enhanced in any other CV so far observed. These abundance patterns are oddly similar to those found for red giants and subgiants in globular clusters (Kraft et al. 1997; Denissenkov et al. 1998; Carretta et al. 2005). Denissenkov et al. believe that such abundance patterns are the natural consequences of hydrogen burning in the CN, NeNa, and MgAl cycles, and that they result from some form of deep mixing that takes material from the hydrogen-burning shell of the red giant and deposits it near the base of the convective envelope. They calculated stellar models to explore the abundance patterns in the radiative layers close to the hydrogen-burning shell and found large abundance and isotopic variations over small changes in radius. Thus, depending on the depth of the mixing, a wide variety of photospheric abundance anomalies are possible. Note that while the masses of the stars they modeled are not too different from the donor stars found in CVs, 0.8 $M_{\odot}$, the metallicities of those objects were much lower than found for any CV ([Fe/H] ∼ −1.5).

While the deep mixing process is not obvious, Denissenkov et al. believe that a rotationally induced instability might be one possible driver. They note that many of the horizontal branch stars in the globular cluster M13, which harbors numerous red giants with peculiar abundances, are rotating much more quickly than seen elsewhere. Given the rapid rotation of CV secondary stars, it does not seem unreasonable to invoke this type of mechanism for those donors that had begun to evolve off the main sequence before entering the mass transfer phase. Alternatively, the apparent increase in the sodium abundance seen in these objects might be due to the failure of using solar abundance pattern atmospheres to generate spectra for objects with reduced levels of hydrogen. If this were the case, however, one would then expect unusual results for other species. The match of the model *JHK* spectra to the data for these objects is excellent throughout the entire spectral range.

The results for sodium, and the presence of magnesium deficits in numerous CVs (RU Peg, and SS Cyg, here), do suggest that some values of [Fe/H] derived in H16 might be suspect. Many of the strongest atomic features in the near-IR spectra of K dwarfs are due to lines of Mg I and Na I. There was no expectation of sodium enhancements in these objects, and thus the χ^2 analysis used in H16 included these features to help limit the values of [Fe/H]. Odd sodium abundances are an even more vexing issue for CVs with M dwarf donors, as the 2.20 μm Na I doublet plays the dominant role in generating [Fe/H] for those objects. Further analysis of the spectra used in H16 will be necessary to explore the extent of this problem.

H16 wondered why only 5 of the 42 CVs discussed in their paper showed CO emission. One of their possible solutions was that CO emission is a transient phenomenon. The new GNIRS observations of RU Peg and SS Cyg show that this might be the correct answer. At no time in the past have we seen CO emission in these two objects; this includes high-resolution Keck NIRSPEC data (e.g., Figures 5 and 10 in Harrison & Hamilton 2015) from which we would have clearly detected it even at the low levels observed here. For objects with lower resolution and/or lower S/N data, it is possible that such very low levels of CO emission could be missed, especially if the emission is asymmetric like that in SS Cyg. In those cases, the value of [C/Fe] will be somewhat larger than derived from fitting synthetic spectra.

T.E.H. and R.E.M. were partially supported by a grant from the NSF (AST-1209451). The Gemini GNIRS data were acquired under the program GN-2016A-Q-55. We acknowledge with thanks the variable star observations from the AAVSO International Database contributed by observers worldwide and used in this research.

References

Arnould, M., Goriely, S., & Jorissen, A. 1999, A&A, 347, 572
Beuermann, K., Baraffe, I., Kolb, U., & Weichhold, M. 1998, A&A, 339, 518
Bitner, M. A., Robinson, E. L., & Behr, B. B. 2007, ApJ, 662, 564
Carretta, E., Gratton, R. G., Lucatello, S., Bragaglia, A., & Bonifacio, P. 2005, A&A, 433, 597
Cushing, M. C., Rayner, J. T., & Vacca, W. D. 2005, ApJ, 623, 1115
Denissenkov, P. A., Da Costa, G. S., Norris, J. E., & Weiss, A. 1998, A&A, 333, 926
Dhillon, V. S., Littlefair, S. P., Marsh, T. R., Sarna, M. J., & Boakes, E. H. 2002, A&A, 393, 611
Echevarría, J., Smith, R. C., Costero, R., Zharikov, S., & Michel, R. 2008, MNRAS, 387, 1563
Figer, D. F., McLean, I. S., & Najarro, F. 1997, ApJ, 486, 420
Gänsicke, B. T., Szkody, P., de Martino, D., et al. 2003, ApJ, 594, 443
Goliasch, J., & Nelson, L. 2015, ApJ, 809, 80
Hamilton, R. T., Harrison, T. E., Tappert, C., & Howell, S. B. 2011, ApJ, 728, 16
Harrison, T. E. 2016, ApJ, 833, 14
Harrison, T. E., Bornak, J., Howell, S. B., et al. 2009, AJ, 137, 4061
Harrison, T. E., & Hamilton, R. T. 2015, ApJ, 150, 142
Hessman, F. V. 1986, ApJ, 300, 794
Howell, S. B., Nelson, L. A., & Rappaport, S. 2001, ApJ, 550, 897
Iben, I., & Livio, M. 1993, PASP, 150, 1373
José, J., & Hernanz, M. 2007, JPhG, 34, R431
Kalomeni, B., Nelson, L., Rappaport, S., et al. 2016, ApJ, 833, 83
Kraft, R. P., Sneden, C., Smith, G. H., et al. 1997, AJ, 113, 279
Kromer, M., Nagel, T., & Werner, K. 2007, A&A, 475, 301
Marks, P. B., & Sarna, M. J. 1998, MNRAS, 301, 699
Podsiadlowski, Ph., Han, Z., & Rappaport, S. 2003, MNRAS, 340, 1214
Politano, M., & Weiler, K. P. 2007, ApJ, 665, 663
Sneden, C. A. 1973, PhD thesis, Univ. Texas
Szkody, P. 1977, ApJ, 217, 140
Thorstensen, J. R., Fenton, W. H., Patterson, J., et al. 2002, PASP, 114, 1117
Wollman, E. R. 1973, ApJ, 184, 773